Journal of Molecular Liquids 429 (2025) 127625

Contents lists available at ScienceDirect

Journal of Molecular Liquids

journal homepage: www.elsevier.com/locate/molliq

# A supramolecular assembly made with sulfobutylether-β-cyclodextrin and magnetic $Fe_3O_4$ showing water remediation properties

Nina Burduja [a,b,1], Giuseppe Nocito [a,1,*], Mariachiara Trapani [a], Alberto Riminucci [c], Riccardo Di Corato [d,e], Antonio Della Torre [d], Angelo Nicosia [f,g], Antonino Gulino [f,g], Placido Giuseppe Mineo [f,g], Antonino Mazzaglia [a,*]

[a] National Research Council, Institute for the Study of Nanostructured Materials (CNR-ISMN) URT of Messina at the Department of Chemical, Biological, Pharmaceutical and Environmental Sciences (ChiBioFarAm), University of Messina – Viale Ferdinando Stagno d'Alcontres, 31 98166 Messina, Italy
[b] Department of Chemical, Biological, Pharmaceutical and Environmental Sciences (ChiBioFarAm), University of Messina – Viale Ferdinando Stagno d'Alcontres, 31 98166 Messina, Italy
[c] National Research Council, Institute for the Study of Nanostructured Materials (CNR-ISMN) Bologna – Via Piero Gobetti, 101 40129 Bologna, Italy
[d] National Research Council, Institute for Microelectronics and Microsystems (CNR-IMM) Lecce – SP Lecce-Monteroni Km 1,200 73100 Lecce, Italy
[e] Center for Biomolecular Nanotechnologies, Istituto Italiano di Tecnologia, Arnesano 73010, Italy
[f] Department of Chemical Sciences, University of Catania – Viale Andrea Doria, 6 95125 Catania, Italy
[g] I.N.S.T.M. UdR of Catania, Viale Andrea Doria, 6 95125 Catania, Italy

ARTICLE INFO

*Keywords:*
Magnetic nanoparticles
Sulfobutylether-β-cyclodextrin
Water remediation
Paraquat

ABSTRACT

In literature many examples of magnetic nanohybrids based on cyclodextrins are reported, but they often require multistep processes and preliminary synthetic efforts that affect the scale-up for the final application. In this paper, a magnetic hybrid system was produced by supramolecular self-assembly between low-cost precursors: the sulfobutylether-β-cyclodextrin (Captisol®) and magnetic iron oxide-based nanoparticles (MNPs). The interaction between the Captisol® and MNPs was elucidated by spectroscopic (Fourier Transform Infrared – FT-IR, X-ray Photoelectron Spectroscopy – XPS, micro X-ray fluorescence – μXRF) and imaging (Transmission Electron Microscopy – TEM) techniques. The resulting MNPs@Captisol assembly was also characterized by thermogravimetric analysis to establish the amount of the organic moiety. The colloidal features were evaluated by dynamic light scattering measurements and an adapted turbidimetric analysis. Finally, a promising use of MNPs@Captisol as remediation agent against paraquat (chosen as a model of cationic pollutant), has been demonstrated. The sequestering mechanism, depending on the concentration and by electrostatic interactions, was ascertained.

## 1. Introduction

The supramolecular approach is based on the self-organisation between specific chemical moieties that interact with each other with the possibility of creating a large library of discrete and ordered non-covalent structures starting from relatively simple precursors [1,2]. Indeed, it is not surprising that this concept – based on large-scale probabilistic and iterative interactions controlled by the laws of thermodynamics – could open to the design of spontaneous but controlled generation of complex matter [3–5]. One of the first tools in supramolecular chemistry has been the host–guest complexation operated by some structures containing cavities capable of binding small molecules [1]. Cyclodextrins (CD) are one of the most studied representants of this family [6]. They are cyclic oligosaccharides obtained from the enzymatic degradation of starch. The most common are constituted by 6 to 8 glucose monomers (α-, β- and γ-CD respectively) joined by α-1,4 glycosidic bonds. They are widely used in drug delivery, environmental science and analytical chemistry to encapsulate some hydrophobic molecules making them dispersible in water [7]. Although the established potentiality, natural cyclodextrins have the drawback of limited aqueous dispersibility. During the last decades, researchers overcame this problem by synthesizing cyclodextrins with extended functionalities

* Corresponding authors.
*E-mail addresses:* giuseppe.nocito@cnr.it (G. Nocito), antonino.mazzaglia@cnr.it (A. Mazzaglia).
[1] These authors contributed equally.

https://doi.org/10.1016/j.molliq.2025.127625
Received 21 December 2024; Received in revised form 11 April 2025; Accepted 18 April 2025
Available online 21 April 2025

such as sulfobutylether-β-cyclodextrin, while maintaining low costs of scale-up production. The functionalization with sulfobutyl chains revealed improved water dispersibility, chemical and enzymatic stability, complexation capability and lower toxicity compared to parent β-CD. Most of these properties are due to the permanent negative charge provided by sulphate groups [8,9]. Recently, an increased interest in the preparation of multifunctional and organic/inorganic hybrid nanomaterials has emerged for their functional aspects on pharmaceutical [10–12], biomedical [13–15], sensing [16] and catalysis [17–19] applications. Hybrid nanomaterials have been described as the connection point between conventional supramolecular chemistry and nanotechnology. In fact, most of their preparation procedures are based on supramolecular aspects as well as on the dynamics of their interaction with the surrounding environment [20]. In this framework, the stabilizing properties of cyclodextrins in the preparation of hybrid materials have been extensively explored [21]. In this context, gold [22–25], bimetallic [26] and magnetic [27] supramolecular assemblies for therapeutic applications have been investigated. Over them, magnetic nanoparticles (MNPs) based on iron oxide have demonstrated relevance for the broadness of applications and properties dependent on precursors, preparation procedure, size, shape, and structure i.e. anisotropy [28]. They have been used as biomedical functional materials for hyperthermia, drug delivery, tissue engineering, and theranostics [29] as well as biosorbents for water remediation application [30]. One of the first use of cyclodextrins with iron oxide nanoparticles was discussed in 2003 by Wang et al [31] in which a phase transfer reaction was performed to pull oleic acid-capped iron oxide nanoparticles to the aqueous compartment in which α-CD was dispersed. From the simple host–guest interaction between oleic acid and α-cyclodextrin, researchers explored increasingly new, complex and fine methods of supramolecular assembly between magnetic nanoparticles and cyclodextrin-based organic layers. β-CD covalently functionalized with citric acid was used for the stabilization of MNPs which were themselves stabilized with Arabic gum [32] or APTES [33]. Recently, Chen et al [34,35] used the citrate strategy to functionalize sulfobutylether-β-cyclodextrin for the stabilization of $Fe_3O_4/SiO_2$ core–shell nanoparticles used for enantioselective liquid–liquid extraction. Lungoci et al [36] used a host–guest complex of sulfobutylether-β-cyclodextrin with protocatechuic acid to stabilize polyethyleneimine-capped MNPs. To the best of our knowledge, there are no reports on the simple supramolecular interaction between sulfobutylether-β-cyclodextrin and MNPs based on non-doped iron oxide ($Fe_3O_4$) producing magnetic hybrids in colloidal dispersion useful for water remediation. In this paper, we will discuss a simple preparation method of a magnetic hybrid based on sulfobutylether-β-cyclodextrin (Captisol®) using trade and low-cost starting materials. The resulting MNPs@Captisol hybrid was characterized by TGA and magnetization identifying the amount of organic coating required for the supramolecular self-assembly. The presence of sulfobutylether-β-cyclodextrin was confirmed by spectroscopic (FT-IR, XPS, μXRF) and morphologic (TEM) analyses. After the evaluation of the colloidal properties from DLS and turbidimetric analysis, promising water remediation properties towards the cationic pollutant molecule paraquat were observed. The sequestering mechanism was related to an electrostatic complexation.

## 2. Materials and methods

### 2.1. Materials

Iron (II,III) oxide nanopowder (50–100 nm particle size, 97 % trace metal basis), paraquat dichloride hydrate (PESTANAL® analytical standard) and methyl orange were provided by Merck Sigma-Aldrich (Milan, Italy). Sulfobutylether-β-cyclodextrin (Captisol®) was a gift from Ligand (San Diego, CA-USA). Ultrapure water (injectable use standard) was purchased from SALF (S.A.L.F. S.p.A. Laboratorio Farmacologico, Cenate Sotto, Italy). A Neodymium permanent magnet (B = 398 mT, F = 63 kgf, 50.8 mm x 50.8 mm x 25.4 mm, MAGFINE SRL, Follonica, Italy) was used for the magnetic settling procedures. A HANNA HI6221-02 (HANNA Instruments, Villafranca Padovana, Italy) pH-meter equipped with HI1093 pH microelectrode was used. For the sonication processes, Elmasonic S 30H (Elma Schmidbauer GmbH, Singen, Germany) ultrasonic bath was used.

### 2.2. Preparation of MNPs@Captisol supramolecular assembly

An ultrapure water stock colloidal dispersion of Captisol® (from here called Captisol) (4.8 mg $mL^{-1}$, 2.219 mM, MW = 2163 g $mol^{-1}$) was prepared by 5 min of sonication at 50 °C. The concentration of MNPs was fixed to 1.2 mg $mL^{-1}$ (5.18 mM for $Fe_3O_4$, MW = 231.54 g $mol^{-1}$) and three different MNPs@Captisol assemblies were prepared at 1:1 w/w, 1:2 w/w and 1:4 w/w ratios or 1:0.1 ($Fe_3O_4$/Captisol) molar, 1:0.21 molar, 1:0.42 molar ratios, respectively. Briefly, Fe(II,III) oxide nanopowder (40.68 mg) was gradually suspended in 33.9 mL of 1.2 mg $mL^{-1}$ (0.555 mM), 2.4 mg $mL^{-1}$ (1.109 mM) and 4.8 mg $mL^{-1}$ (2.219 mM) Captisol aqueous dispersions, respectively. The 1.2 mg $mL^{-1}$ and the 2.4 mg $mL^{-1}$ dispersions were prepared from the dilution of the 4.8 mg $mL^{-1}$ stock. After each addition the reaction mixture was mechanically stirred by vortex for 1 min and, when the final volume was reached, nitrogen flow was bubbled for 5 min. The MNPs@Captisol assemblies were purified from the unreacted by magnetic settling for 10 min discarding the supernatant. The precipitate was washed two times in ultrapure water following the magnetic settling procedure and finally dried in a vacuum oven at 30 °C overnight. The resulting powders were used for thermogravimetric analysis and magnetic characterizations. The MNPs@Captisol 1:1 w/w assembly - from here called MNPs@Captisol - was further characterized (XPS, FT-IR, TEM, μXRF, DLS) and was used for the water remediation experiments. The assembly was reconstituted in ultrapure water as follows: a 1 mg $mL^{-1}$ suspension of MNPs@Captisol was prepared through 1 min of sonication followed by 5 min of vortex mixing and serially 1:2 diluted to obtain stable dispersion at 82 μg $mL^{-1}$, 62.5 μg $mL^{-1}$ and 41.67 μg $mL^{-1}$. For each dilution, the sonication/mixing protocol was repeated as for the first step.

### 2.3. Water remediation

The water remediation behaviour of MNPs@Captisol was compared with pristine MNPs *vs.* a positive-charged water pollutant (paraquat) and a negative-charged pollutant dye (methyl orange). Briefly, 10 mL of 82 μg $mL^{-1}$ and 62.5 μg $mL^{-1}$ ultrapure water dispersions of MNPs@Captisol and MNPs were placed into a 100 mm glass Petri dish, separately. After that, a small volume (100 μL, 150 μL, 200 μL) of a concentrated stock solution of the analyte to be removed (1 mM) was added to get the final 10 μM, 15 μM or 20 μM samples, respectively. Then, they were gently shaken in an orbital oscillator for 40 min and placed over a Neodymium permanent magnet for 20 min to separate the precipitate where the analyte was adsorbed from the clear supernatant containing the unreacted. In the end, the process was repeated until reaching 80 min of interaction. The amount of analyte sequestered by the systems was spectrophotometrically estimated by subtracting the absorption of the supernatant from the absorption of the reference solution. Results were plotted as absorption differences divided by absorption of the reference solution $\Delta A/A_0$ over time.

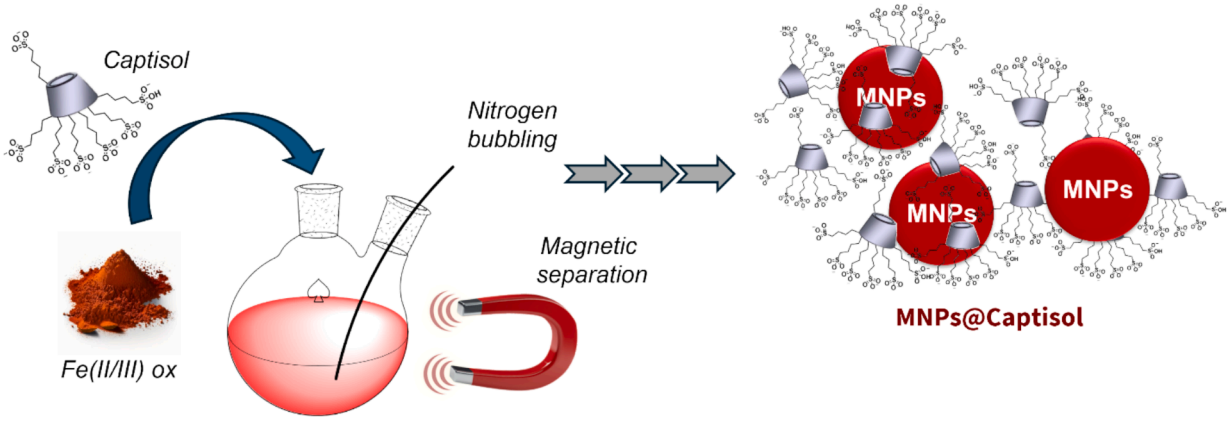


**Fig. 1.** MNPs@Captisol preparation procedure scheme.

### 2.4. Characterizations

#### 2.4.1. Thermogravimetric analysis (TGA)

The TGA analyses were performed using a Perkin-Elmer (Perkin-Elmer Inc., Waltham, MA-USA) TGA7 equipped with a TAC 7/DX digitizer. The measurements were performed in air atmosphere (60 mL $min^{-1}$), in the 50–800 °C range with a thermal ramp of 10 °C $min^{-1}$. Degradation temperatures were measured as onset temperature of the TGA trace.

#### 2.4.2. Optical spectroscopy (UV/Vis and FT-IR)

UV/Vis absorption spectra were recorded in air equilibrated 1 cm quartz cell at 25 °C with a Jasco (Jasco Co., Tokyo, Japan) V-770 UV/Vis-NIR double beam scanning spectrophotometer equipped with a Peltier temperature control system. FT-IR spectra were acquired thanks to the Attenuated Total Reflectance (ATR) technique in a Jasco (Jasco Co., Tokyo, Japan) FT/IR-4X spectrophotometer equipped with single-reflection ATR accessory with a diamond prism.

#### 2.4.3. X-ray Photoelectron spectroscopy (XPS)

X-ray photoelectron spectra were measured at 45° take-off angle relative to the surface sample holder, with a PHI 5000 Versa Probe II system (ULVAC-PHI Inc., Chigasaki, Japan) set to have the base pressure of the main chamber $1 \bullet 10^{-8}$ Pa [37,38]. Samples were excited with the monochromatized Al Kα X-ray radiation using a pass energy of 5.85 eV. The instrumental energy resolution was ≤ 0.5 eV. The XPS peak intensities were obtained after Shirley background removal. Spectra calibration was achieved by fixing the Ag $3d_{5/2}$ peak of a clean sample at 368.3 eV. This method turned the C 1 s peak of the adventitious carbon contamination at 285.0 eV [37,39]. The atomic concentration analysis was performed by considering the relevant atomic sensitivity factors. The fitting of some XP spectra was carried out using the XPSPEAK 4.1 software by fitting the spectral profiles with symmetrical Gaussian envelopes, after subtraction of the background. The Fe 2p spectrum was fitted using $2p_{3/2} - 2p_{1/2}$ spin–orbit components in a fixed 2:1 intensity ratio. This process involves data refinement, based on the method of the least squares fitting, carried out until there was the highest possible correlation between the experimental spectrum and the theoretical profile. The residual or agreement factor R defined by $R = \sqrt{(F_{obs} - F_{calc})^2 / \sum (F_{obs})^2}$ after minimization of the function $\sum (F_{obs} - F_{calc})^2$ converged to the value of 0.03.

#### 2.4.4. Dynamic light scattering (DLS) analysis

The mean hydrodynamic diameter ($D_H$), width of distribution (polydispersity index, PDI) and ζ-potential were measured with Malvern Zetasizer Nano ZS (Malvern Instruments, Malvern, UK) equipped with a He-Ne laser (λ = 633 nm, power = 4 mW). Measurements were performed using the non-invasive backscattering technique (NIBS) with an angle of 173° to the incident beam, 45 acquisitions at a temperature of 25 ± 1 °C for each measurement were collected. Deconvolution of the measured correlation curve (distribution of relaxation times and the cumulant analysis) into a dimensional average intensity distribution was obtained using the Laplace inversion algorithm. All the colloidal dispersions were freshly prepared at 25 °C before performing the DLS analysis.

#### 2.4.5. Colloidal stability

The colloidal stability of MNPs@Captisol and bare MNPs was evaluated with an adapted turbidimetric method at 25 °C and in ultrapure water dispersion. Samples were prepared at 82 μg $mL^{-1}$, 62.5 μg $mL^{-1}$ and 41.67 μg $mL^{-1}$ and immediately placed in a 1 cm quartz cuvette inside the Peltier temperature-controlled UV/Vis spectrophotometer. Experiments were performed recording the extinction values at 790 nm every 10 min in a time interval from 0 to 300 min. Results were plotted against time and fitted using the OriginPro 2021 software with the equation $y = y_0 + Ae^{R_0 x}$ for a first-order exponential decay model where $R_0$ is the rate constant, and $x$ is the time. Samples were compared for their half-life $t_{1/2}$ calculated from the following formula $t_{1/2} = \ln 2 / -R_0$. Results were associated with the DLS evaluation of the mean hydrodynamic diameter ($D_H$) recorded every 30 min until 120 min.

#### 2.4.6. Magnetic characterization

A custom-built Faraday magnetometer was used to measure the magnetic moment per unit mass (σ value) of the samples as a function of the applied field at 27 °C [40]. The magnetometer is based on a Sartorius ME235S (Sartorius AG, Göttingen, Germany) analytical balance and a NdFeB permanent magnet, with a maximum applied magnetic field of 0.12 T.

#### 2.4.7. Transmission electron Microscopy (TEM)

TEM analysis of bare MNPs and MNPs@Captisol was performed with a JEOL JEM-1011 (JEOL Ltd., Tokyo, Japan) transmission electron microscope at 100 keV operating voltage, equipped with a 7-megapixel CCD camera (Orius SC600A, Gatan, Pleasanton, CA-USA). TEM image

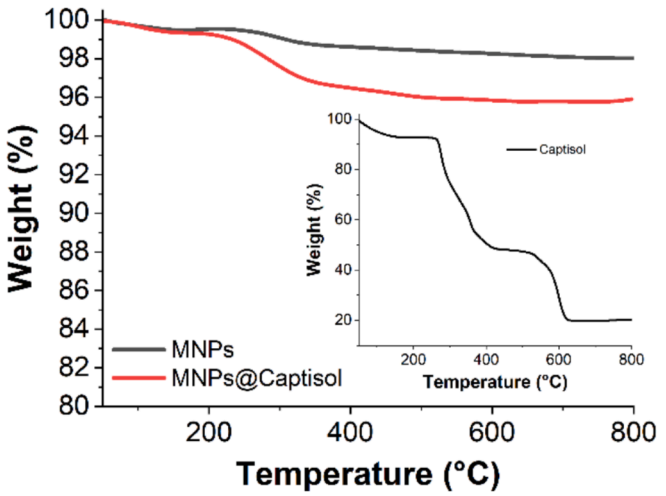


**Fig. 2.** Thermogravimetric traces (air atmosphere) of MNPs, MNPs@Captisol 1:1 w/w. In the inset, the TGA trace of Captisol (air atmosphere).

analysis was achieved with Gatan Digital Micrograph™ (DM) software. For the sample preparation, a few microliters of MNP suspension were dropped onto carbon-coated copper grids.

#### 2.4.8. Micro X-ray fluorescence (μXRF) analysis

μXRF measurements (Orbis PC Micro-XRF system, Edax/Ametek, Mahwah, NJ-USA) were performed, under a vacuum condition with a scanning area of 0.66 x 0.66 mm, on dried spots of Captisol and MNPs@Captisol, obtained by drop-casting on polyimide substrates. The measurements were carried out with the time constant of 12.8 μs, dwell time of 400 ms and matrix size of 32 × 25 pixels, using 30 kV of beam voltage, 400 μA of beam current and a spot size of 30 μm. The target anode in the X-Ray tube is made in rhodium and a silicon/lithium detector was used to collect the characteristic X-ray emitted by the sample.

## 3. Results and discussion

### 3.1. Material preparation

This work aimed to study the supramolecular assembly processes between $Fe_3O_4$ (magnetite) nanopowder – widely used in many industrial or manufacturing processes, as in the production of pigments and ceramics or for heterogeneous catalysis – and sulfobutylether-β-cyclodextrin (Captisol) an anionic β-cyclodextrin derivatized with sulfobutyl chains (see Fig. 1).

Captisol was designed and synthetised between the late 1980s and early 1990s to improve water dispersibility, chemical and enzymatic stability and biocompatibility concerning native β-cyclodextrin. These properties come from the permanent negative charge provided by the sulfonic groups that are in the ionized form at all relevant pH values [9]. Nowadays, due to industrial production and the broad spectrum of applications led by the pharmaceutical Captisol is considered one of the cheapest and most known anionic β-cyclodextrin derivatives. In literature, there are some examples of the use of cyclodextrins to stabilize iron oxide nanoparticles but they often use multistep processes and preliminary synthetic efforts. In this work, it was decided to evaluate the natural stabilizing ability of sulfobutylether-β-cyclodextrin for pristine iron oxide nanoparticles (MNPs). Considering the final application which potentially requires a large amount of adsorbing species and therefore an easy scale-up, the aim was to optimize time, costs and efforts to produce a magnetic system useful for water remediation. Due to the lack of comprehensive and detailed references, it was studied for the first time the self-assembly between iron oxide nanoparticles and Captisol producing the MNPs@Captisol system. To understand the reaction

**Table 1**
TGA experimental results (depicted as wt %) for MNPs@Captisol assemblies (depicted as the w/w ratio used in the preparation) and the MNPs and Captisol precursors.

| *Sample* | *Residue at 800 °C* | *Weight Loss at 800 °C* | *Loading* |
|---|---|---|---|
| Captisol | 20.35 | 79.65 | – |
| MNPs | 98.02 | 1.98 | – |
| MNPs@Captisol (1:1) | 95.90 | 4.10 | 2.73 |
| MNPs@Captisol (1:2) | 95.87 | 4.13 | 2.77 |
| MNPs@Captisol (1:4) | 95.96 | 4.04 | 2.65 |

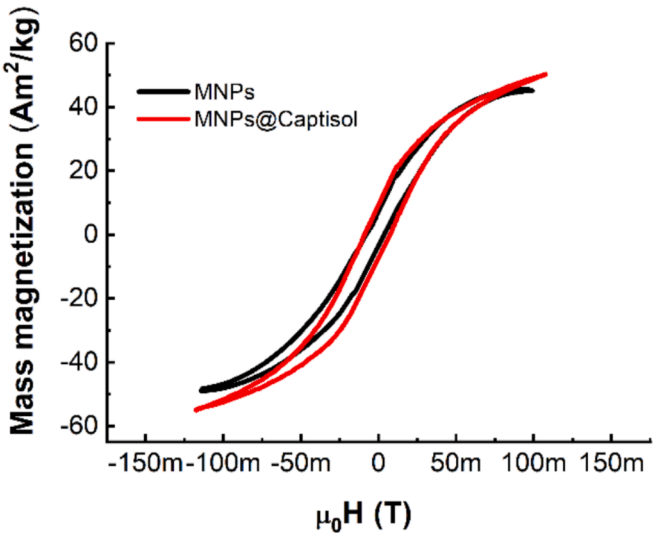


**Fig. 3.** Mass magnetization hysteresis loops of MNPs@Captisol and MNPs.

stoichiometry, the concentration of MNPs was fixed to 1.2 mg $mL^{-1}$ (5.18 mM if approximating $Fe_3O_4$ as the main constituent of MNPs), thus varying the Captisol amount. In particular, three different ratios were experimentally evaluated: 1:1 w/w (1:0.1 $Fe_3O_4$/Captisol molar ratio), 1:2 w/w (1:0.21 molar ratio) and 1:4 w/w (1:0.42 molar ratio). The magnetite was dispersed per step in the corresponding dispersion of Captisol (1.2 mg $mL^{-1}$ – 0.555 mM, 2.4 mg $mL^{-1}$ – 1.109 mM and 4.2 mg $mL^{-1}$ – 2.219 mM) using vortex agitation, short sonication time and nitrogen bubbling. Note that the 1.2 mg $mL^{-1}$ concentration of MNPs was a good compromise between dispersibility and minimization of the reaction volume that preserved the reactivity without affecting laboratory scale manipulability. The material was purified from the unreacted cyclodextrin by magnetic settling. The clear supernatant was removed, and the precipitate was washed twice in ultrapure water following the magnetic settling procedure. The procedure is reported in Fig. 1. Finally, the collected solid was dried overnight under vacuum at 30 °C. Further characterizations such as thermogravimetric analysis and mass magnetization hysteresis loops were used to check the reaction product (*see paragraphs 3.2 and 3.3*).

### 3.2. Thermogravimetric analysis (TGA)

The amount of Captisol on the 1:1 w/w, 1:2 w/w and 1:4 w/w MNPs@Captisol assemblies, that is to say the amount that interacted with MNPs during the self-assembly reaction, was evaluated by thermogravimetric analysis in an air atmosphere.

The TGA of Captisol (inset of Fig. 2) shows a multi-step degradation path: the first step, ending at about 200 °C (~ 7.4 % weight loss) is due to the release of the adsorbed water; the second step occurs from approximately 264 °C to 460 °C, associated with a weight loss of ~ 45 wt %; the final step (~ 28 % loss) occurs from about 529 °C to 630 °C, leaving a residue at 800 °C of about 20 wt %. According to the literature

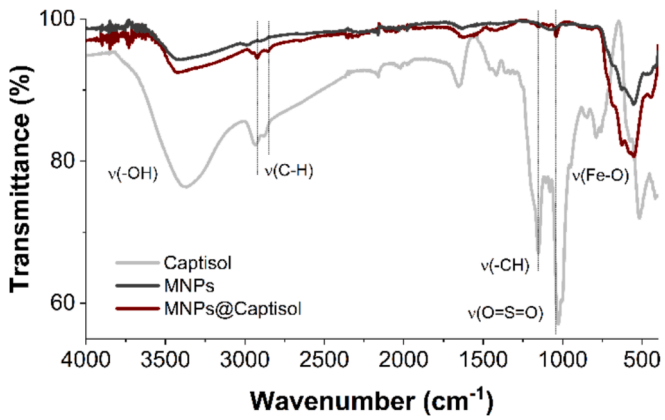


**Fig. 4.** ATR FT-IR spectra of pristine MNPs, Captisol (sulfobutylether-β-cyclodextrin) and MNPs@Captisol assembly.

[17], the second step is attributed to a partial degradation of the β-CD core and the sulfobutylether moiety. The third degradation step could be associated with the final oxidation of residual organic matter. The TGA profile of MNPs showed continuous weight loss up to 800 °C leaving a residue of approximately 98 wt %. Finally, the thermal profiles of MNPs@Captisol samples 1:1 w/w, 1:2 w/w and 1:4 w/w were similar to each other (for brevity, Fig. 2 reports only the TGA trace of the sample MNPs@Captisol 1:1 w/w; the TGA traces of the 1:2 w/w and 1:4 w/w samples are reported in Fig. S1), showing a decomposition process occurring from 230 °C to 350 °C, which is compatible with the Captisol degradation, leaving a residue of around 96 wt %. Taking into account the weight losses at 800 °C of pure MNPs and Captisol, the amount of Captisol in MNPs@Captisol samples resulted in approximately 2.7 wt %. Noticeably, preparations starting from a higher amount of Captisol (1:2 w/w and 1:4 w/w) resulted in a final loading similar to the 1:1 w/w ratio (see Table 1).

This data suggests that, probably, the maximum loading depends on the footprint of the Captisol which, due to hysteric hindrance, does not allow a higher CD-derivative assembly on MNPs. To verify this hypothesis, magnetic characterizations were performed for all the samples to confirm if the organic layer coating was different between the samples (*see paragraph 3.3*).

### 3.3. Magnetic characterization

The mass magnetization hysteresis loops of the MNPs@Captisol 1:1 w/w and pristine MNPs are reported in Fig. 3.

They showed a coercivity of approximately 8 mT. The value was similar to that found in a previous work from our research group in which the same precursor was used [27]. The measured ferromagnetism indicates that the mean size of the MNPs is greater than the superparamagnetic limit (critical diameter 10 nm [41]), as confirmed by TEM micrographs in Fig. 6A. This could cause aggregation of the MNPs due to the dipolar interaction [42]. This interaction occurs when each particle is fully magnetized and when its diameter is greater than the superparamagnetic limit. In this work, the dimension of the magnetite nanoparticles correspond to a single magnetic domain [43,44] meaning that each MNP is fully magnetized. In summary, in MNPs the dipolar interaction, which could cause aggregation, is always present. Despite this, no aggregation occurred as demonstrated by the DLS measurements reported in Table 2 (*see paragraph 3.6*). The mass magnetization is similar between pristine MNPs and the MNPs@Captisol 1:1 w/w, 1:2 w/w and 1:4 w/w samples (47 $Am^2/kg$ and 50 $Am^2/kg$ at 100 mT, respectively) as reported in Fig. S2. The small difference is justified by the small weight contribution of the organic part in the supramolecular assemblies (approximately 2–3 %), as demonstrated by TGA (*see paragraph 3.2*). The MNPs@Captisol 1:4 w/w (Fig. S2) was the only sample in which the mass magnetization decreased significantly from the value of the pristine MNPs. Together with the fact that the average covering percentage of Captisol (*see again TGA in paragraph 3.2*) was almost unaffected by the preparation conditions, we confirmed the hypothesis to

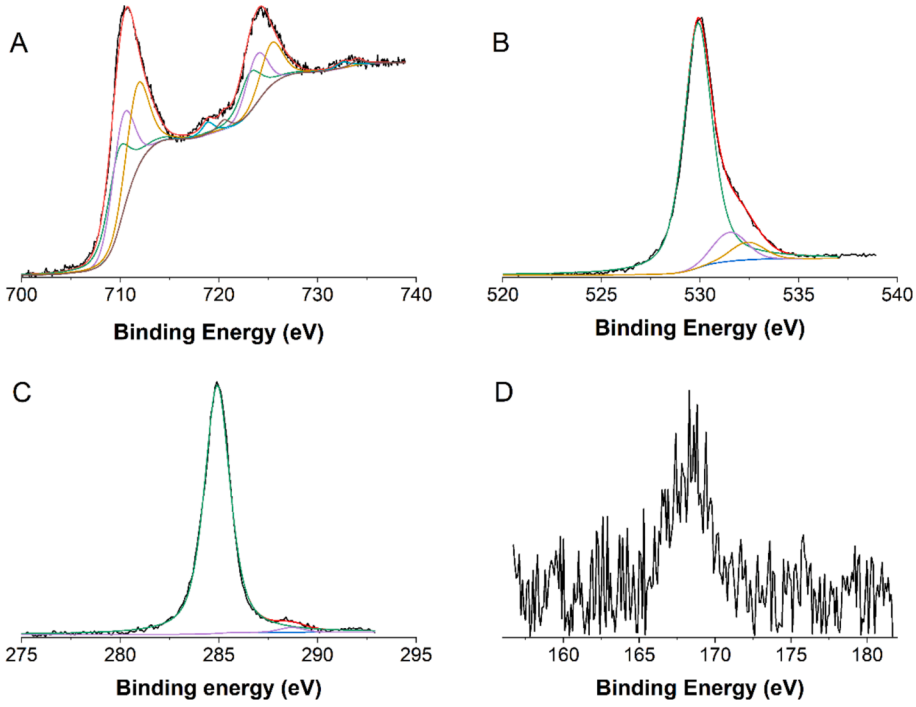


**Fig. 5.** Al-Kα excited XPS of the MNPs@Captisol assembly in the following binding energy regions: A) Fe 2p – the green, violet, yellow, light blue and brown lines refer to the 709.6, 710.5, 712.4, 718,9 and 720.5 eV components, respectively; B) O 1 s – the green, violet and yellow lines refer to the 529.9, 531.5 and 532.4 eV components, respectively; C) C 1 s – the green and violet Gaussians refer to the 285.0 and 288.7 eV components, respectively; D) S 2p. The blue line refers to the background and the red line superimposed to the black experimental profile refers to the sum of all the Gaussian components.

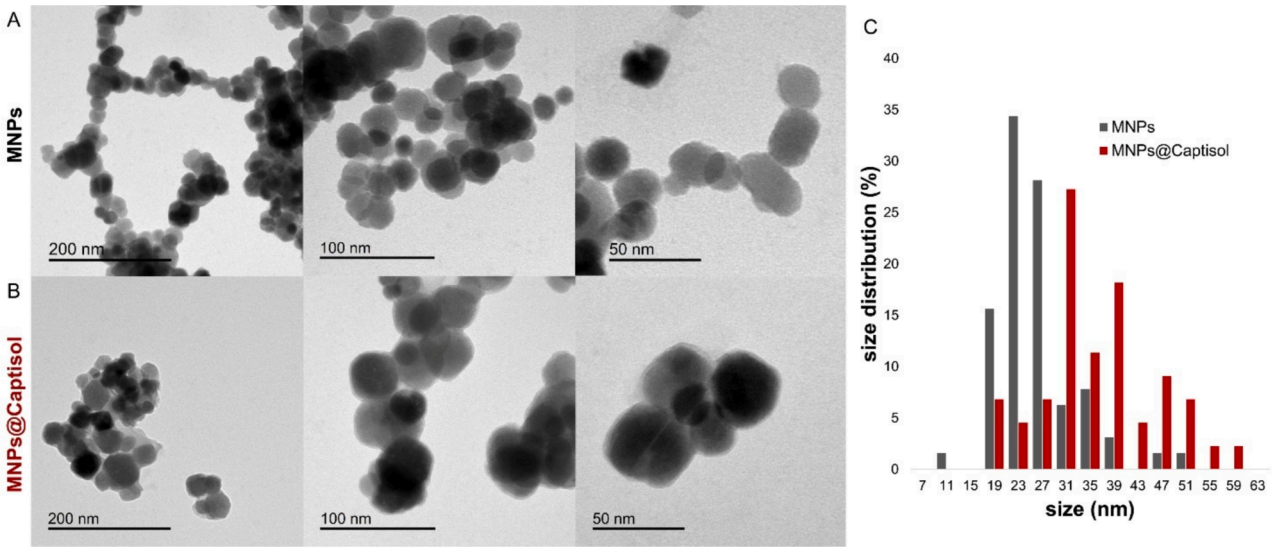


**Fig. 6.** TEM images of A) MNPs and B) MNPs@Captisol assembly. C) Size distribution analysis on the TEM images of MNPs and MNPs@Captisol in Fig. 6A and 6B, respectively.

continue further characterizations and experiments with the MNPs@Captisol 1:1 w/w assembly.

### 3.4. Spectroscopic characterizations: FT-IR and XPS

The FT-IR spectra of MNPs, MNPs@Captisol and Captisol are depicted in Fig. 4.

The spectrum of bare MNPs reveals the characteristics peaks of $Fe_3O_4$ nanostructures with the stretching vibrations associated with Fe-O bonds in the 570–630 $cm^{-1}$ range, together with the vibrations of hydroxyl groups coming from both the adsorbed water and the surface functionalization of the particles at 1626 $cm^{-1}$ and on the 3000–3500 $cm^{-1}$ interval for bending and stretching modes, respectively [45]. The spectrum of Captisol showed clearly the absorption bands of the –OH groups present both on the outer face of the cyclodextrin and on the adsorbed water, for the stretching (3700–3100 $cm^{-1}$) and bending (1645 $cm^{-1}$) vibrations found. Moreover, the absorption peaks at 2935 $cm^{-1}$ and 2876 $cm^{-1}$ for −C–H symmetric and asymmetric stretching, at 1150 $cm^{-1}$ for –CH stretching and at 1028 $cm^{-1}$ for O=S=O stretching confirmed the presence of sulfobutylether chains as surface functionalities [46]. On the MNPs@Captisol spectrum, the absorption patterns of magnetite were visibly maintained in addition to the sulfobutylether chains peaks from the Captisol precursor. In particular, the O=S=O stretching peak was found to be shifted to 1043 $cm^{-1}$, unless for the –CH stretching peak that remained unaltered in position. A similar but slighter shifting trend was detected for the −C–H stretching peaks that in the assembly were at 2921 $cm^{-1}$ and 2853 $cm^{-1}$. The broad –OH stretching band was closely remembering the shape of the MNPs precursor one. This advised that the process of supramolecular assembly between MNPs and sulfobutylether-β-cyclodextrin occurred. Concerning the precursor, the hiding of the –OH groups in the MNPs@Captisol spectrum suggests an alteration of the cyclodextrin conformation which might be also explained by a lower amount of adsorbed water which is also evidenced by the broadening of its bending vibration band at ~ 1650 $cm^{-1}$.

The IR spectroscopy suggested the supramolecular interaction between the precursors, so it was continued investigating the electronic configuration of the surface atoms of the MNPs@Captisol system through X-ray Photoelectron Spectroscopy (XPS). This powerful technique displayed the dynamics of the assembly thus confirming the presence of stable interactions between Fe atoms and $SO_3^-$ groups from the sulfobutylether chains of Captisol together with the other Captisol contributions in the high-resolution O 1 s and C 1 s spectra reported in Fig. 5. The survey spectrum of MNPs@Captisol is reported in Fig. S3.

The $Fe_3O_4$ spinel structure is represented by a cubic close packing of $O^{2-}$ ions where iron shows both $Fe^{2+}$ and $Fe^{3+}$ oxidation states, being $Fe^{2+}$ in octahedral sites and $Fe^{3+}$ in both octahedral and tetrahedral sites. All Fe ions are in high spin configurations. Fig. 5A shows the high-resolution XPS in the Fe 2p binding energy region. A careful fitting of the experimental spectrum required five Gaussian doublets whose Fe $2p_{3/2}$ components are at 709.6 eV, 710.5 eV, 712.4 eV, 718.9 eV, 720.5 eV that were assigned to $Fe^{2+}$ in octahedral sites, $Fe^{3+}$ in octahedral sites, $Fe^{3+}$ in tetrahedral sites, $Fe^{3+}$ in surface sites and a shake-up satellite peak due to $Fe^{2+}$ in octahedral sites, respectively [47]. At 13.6 eV higher binding energy all these peaks show the Fe $2p_{1/2}$ components. These results agree well with already reported data for $Fe_3O_4$ and with the XPS data of the pristine MNPs ($Fe_3O_4$) used in the present study for comparison (Fig. S4) [47–50]. After fitting, the XPS Fe 2p components of the three iron states were found in the almost nominal 1.03:1.03:1 intensity ratio. Moreover, as stated in the experimental paragraph, the fitting procedure imposed the $2p_{3/2}/2p_{1/2}$ intensity ratio = 2. Fig. S5 shows the same spectrum after the subtraction of the background and the ~ 1:1:1 iron state intensity ratio is much more evident. The XPS spectrum in the O 1 s core level binding energy (Fig. 5B) shows three bands at 529.9 eV, 531.5 eV and 532.4 eV corresponding to ionizations of Fe-$O_{lattice}$, C-O-C (ether)/OR (alkoxy) and $SO_3$-Fe states. This B.E. value agrees well with those measured for a similar system [27]. In addition, Fig. S6 shows the XPS spectrum of the pristine MNPs in the O 1 s core level binding energy, for comparison. In Fig. 5C, the high-resolution spectrum in the C 1 s binding energy region shows a rather symmetric band centered at 285.0 eV, even though a careful fitting of the experimental spectrum required an additional small intensity band at 288.7 eV. The main band is due to the aliphatic carbon states and the additional band agrees with the ionizations of the Fe-$O_2$CR states. Fig. S7 shows the XPS of the Captisol

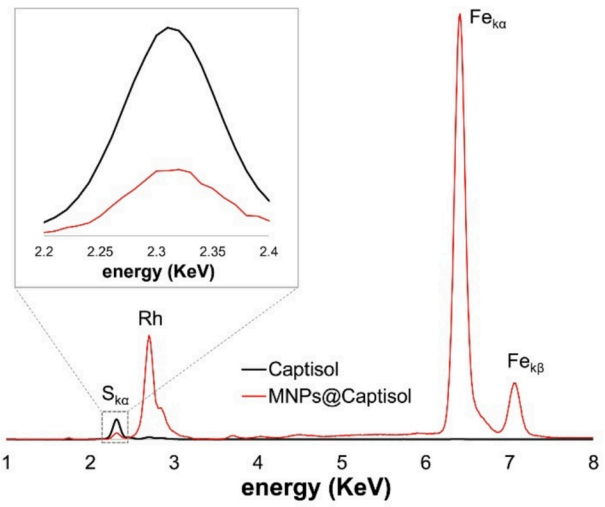


**Fig. 7.** μXRF analysis of Captisol and MNPs@Captisol. In the figure inset, a magnification of the sulfur peak area is reported.

in the C 1 s binding energy region, for comparison. In this latter case, apart from the main band at 285.0 eV, there is evidence of a strong intensity band at 286.3 eV, consistent with the C-OR states and of additional, low intensity, higher binding energy, shoulders due to the −C=O states (287.5 eV) and some $-CH_2SO_3^-$ states (288.7 eV). Finally, the XPS in Fig. 5D in the S 2p binding energy region is characterized by a noisy but evident signal that appeared at 168.3 eV confirming the presence of sulphate $-CH_2SO_3^-$ states.

### 3.5. Transmission electron Microscopy (TEM) imaging and μXRF analysis

In Fig. 6, representative images from TEM characterization are depicted.

The morphology of MNPs@Captisol assembly in Fig. 6B is represented by clusters of iron oxide nanoparticles – in which the number of individual constituents is variable – that are surrounded by a thin organic layer, as can be seen from the presence of less electrodense areas surrounding the more electrodense ones in the images. From the statistical analysis (Fig. 6C), the overall size was calculated at 32.2 ± 9.5 nm and only a slight polydisperse distribution was found. The inorganic core, constituted by the MNPs had an average dimension of 26.2 ± 6.6 nm, indeed the organic layer was 2.54 ± 0.6 nm in thickness. Moreover, compared to the pristine MNPs an improvement in the stability of the system can be observed which is reflected by the decrease in aggregation. The same is not observed in Fig. 6A where pristine MNPs showed a higher degree of aggregation creating very compact clusters rich in iron oxide nanoparticles. Furthermore, there was no trace of organic matter/layers in the proximity of iron oxide clusters.

To further characterize the MNPs@Captisol assembly at the atomic composition level, the μXRF technique was used to perform mapping of the elements from single spot analysis detecting characteristic X-rays emitted by the sample from the interaction with primary X-rays. The operating conditions (beam voltage and current, filter usage and beam spot size) affecting the sensitivity and accuracy of the technique were calibrated for the detection of sulfur. From the measurements of the MNPs@Captisol and Captisol samples, the sulfur peak was observed downstream of the primary beam Rh(L) lines (Fig. 7).

Results showed that the signal-to-noise ratio for the Skα peak improves when the analysis is performed at higher voltages in the 20 – 40 kV range. This is probably due to a shift of the bremsstrahlung radiation towards higher energies, thus giving more pronounced signals in the collected spectrum. For the different voltage values used, the sulfur peak of the MNPs@Captisol was detected at the same energy as the Captisol one, unambiguously confirming the presence of this element in MNPs@Captisol. Moreover, the presence of Fe is due to the inorganic core composition (iron oxide) of the MNPs@Captisol.

### 3.6. Colloidal properties: DLS analysis and stability

The effect of the supramolecular assembly between MNPs and Captisol was evaluated by dynamic light scattering (DLS) analysis estimating the mean hydrodynamic diameter ($D_H$) and the ζ-potential of the particles upon ultrapure water dispersion. The stability of the system was evaluated by performing an adapted turbidimetric analysis associated with the $D_H$ observations. Considering that the more stable sample had a half-life of 50 min, the variations in the $D_H$ were analysed until 120 min. The colloidal properties of MNPs and MNPs@Captisol were investigated for three concentrations (82 μg mL$^{-1}$, 62.5 μg mL$^{-1}$ and 41.67 μg mL$^{-1}$) where samples showed better dispersion by visual inspection. Complete characterizations are reported in the supporting information from Fig. S8 to Fig. S16 and from Table S1 to Table S3. When in dispersion, bare MNPs showed polydispersity with multiple $D_H$ around 120 nm and 550 nm together with some non-correlated larger aggregates whose abundance was ≤ 5 % (see the t = 0 values in Tables S1-S3 for 82 μg mL$^{-1}$, 62.5 μg mL$^{-1}$ and 41.67 μg mL$^{-1}$ dispersion, respectively). Over time, the intensity values of the populations balanced each other (see Fig. S9, Fig. S12, Fig. S15). Samples had appreciable stability, as suggested by the half-life values extrapolated by the turbidimetric traces between 45 and 50 min (see Fig. S8A, Fig. S11A, and Fig. S14A). ζ-potential values around + 30 mV were recorded in accordance with the literature [51] where similar magnetite nanoparticles showed positive ζ-potential at pH 5.5–6. Compared to MNPs, the dispersions of MNPs@Captisol were more homogeneous and monodisperse. In addition, the average $D_H$ of around 1 μm was generally maintained over time (see Fig. S10, Fig. S13 and Fig. S16). Thus, the stability was reduced finding turbidimetric half-life values between 25 and 29 min (see Fig. S8B, Fig. S11B, and Fig. S14B) as corroborated by the essential electroneutrality between the solvation spheres of the particles (ζ-potential). It must be noticed that the inversion of the ζ-potential is another strong evidence of the interaction of the negatively charged Captisol molecules with the positively charged MNPs. 2 μg mL$^{-1}$ (~ 1 μM) pure Captisol dispersion (pH 6.2) was prepared following the same protocol for MNPs@Captisol assembly preparation and analysed showing a monodisperse system of around 370 nm with a ζ-potential value of −8 mV – accordingly to previously published reports [52,53] and to the value of MNPs@Captisol – demonstrating the possibility of the system to hybridize with positively charged nano/microparticles (results in Table 2). The 2 μg mL$^{-1}$ concentration was the closest amount of Captisol in the MNPs@Captisol assembly considering the ~ 3 wt% covering percentage experimentally found by TGA.

**Table 2**
Colloidal properties from DLS analysis and adapted turbidimetric method in ultrapure water of freshly prepared samples at 25 °C. Average hydrodynamic diameter ($D_H$), Polydispersity Index (PDI), ζ-potential (ζ), standard deviation (S.D.).

| *Sample* | *$D_H$ (nm ± S.D.)* | *PDI* | *ζ-potential (mV ± S.D.)* | *Half-life* [a] *($t_{½}$)* |
|---|---|---|---|---|
| Captisol | 379 ± 112 | 0.09 | −8 ± 5 | – |
| MNPs | 562 ± 214 (81)<br>125 ± 30 (13) | 0.14<br>0.05 | +28 ± 6 | 50 min |
| MNPs@Captisol | 829 ± 129 | 0.03 | −9 ± 5 | 28 min |

[MNPs@Captisol] = [MNPs] = 62.5 μg mL$^{-1}$, [Captisol] ~ 2 μg mL$^{-1}$.
PDI was calculated from the single peak using the following equation $PDI = S.D.^2/D_H^2$
A larger and aggregated fraction ($D_H$ ~ 4–5 μm, abundance ≤ 5%) was found in MNPs and MNPs@Captisol samples but not included in the table.
[a] The stability of the dispersion was evaluated plotting the extinction values at 790 nm vs. time and fitting with a first-order exponential decay equation where the half-life value was calculated.

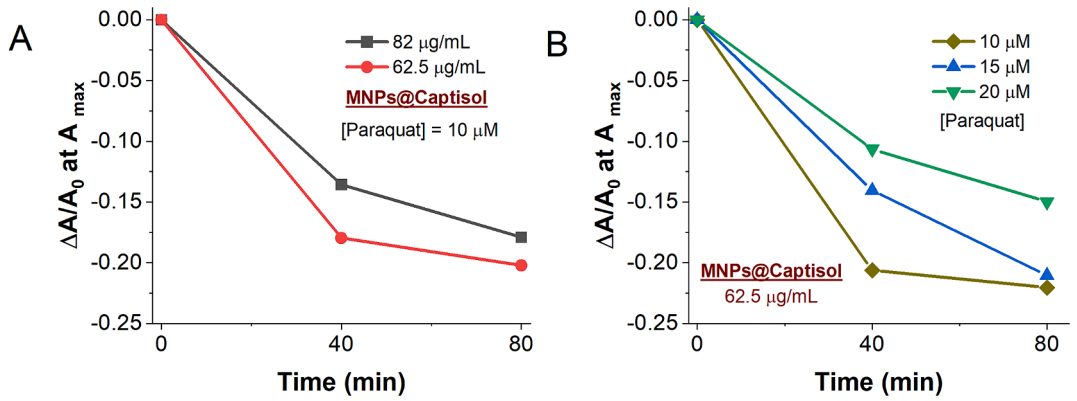


**Fig. 8.** Concentration and time dependent water remediation experiments reported as absorbance differences at the absorbtion maximum of paraquat (258 nm) as a function of time (min). A) [Paraquat] = 10 μM, [MNPs@Captisol] = variable (82 μg $mL^{-1}$ and 62.5 μg $mL^{-1}$); B) [MNPs@Captisol] = 62.5 μg $mL^{-1}$, [Paraquat] = variable (10 μM, 15 μM and 20 μM).

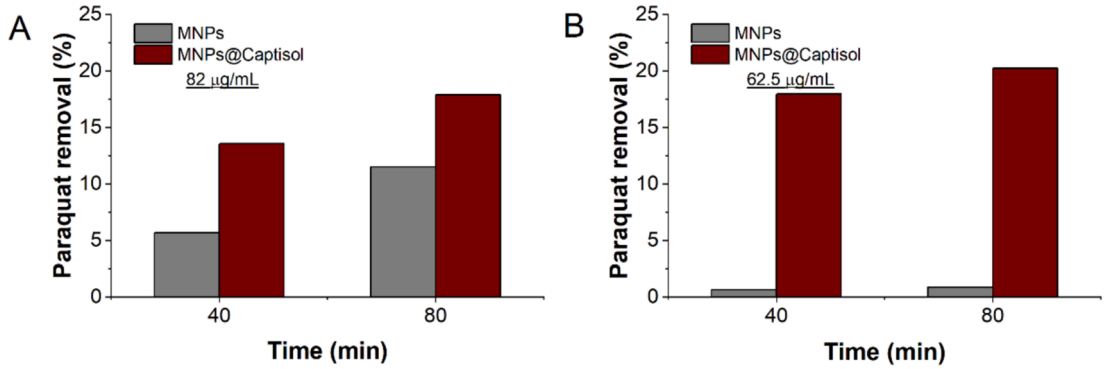


**Fig. 9.** Comparison of concentration and time dependent water remediation experiments between MNPs@Captisol (red bar) and MNPs (gray bar) reported as paraquat removal percentages as a function of time (min), [Paraquat] = 10 μM. A) 82 μg $mL^{-1}$; B) 62.5 μg $mL^{-1}$.

Nonetheless the apparent negligible extent, looking at the differences between the three investigated concentrations, a pseudo-linear stability dependence by the concentration was perceived. Hence, both because it is the average and because of the following experimental results on water remediation (*see paragraph 3.7*) the representative concentration for MNPs and MNPs@Captisol systems was 62.5 μg $mL^{-1}$ and results are elucidated in Table 2.

### 3.7. Water remediation

The MNPs@Captisol supramolecular assembly demonstrated preserved magnetic properties compared to pristine MNPs, good aqueous dispersibility and colloidal stability. Therefore, its behaviour towards water remediation was explored. Paraquat dichloride was selected as a water pollutant model. It is extremely effective in weed control but toxic as well for humans as it is rapidly sorbed by soils where it is persistent also down to groundwater, without any external inactivation [54]. Time and concentration-dependent experiments were performed to assess the water remediation properties of the assembly. The concentration interval of MNPs@Captisol was investigated at 62.5 μg $mL^{-1}$ and 82 μg $mL^{-1}$. The absorption capability of paraquat was performed at 40 min and 80 min. To separate the MNPs@Captisol/paraquat adduct from the free paraquat, the dispersion was magnetic settled for 20 min and the clear supernatant solution was spectrophotometrically analysed. The same protocol was carried out with pristine MNPs, as control experiments.

As reported in Fig. 8A, keeping fixed the concentration of paraquat at 10 μM, the sample with the 62.5 μg $mL^{-1}$ concentration of MNPs@Captisol was more efficient than the 82 μg $mL^{-1}$ one. In particular, the 82 μg $mL^{-1}$ sample sequestered ~ 13 % of paraquat at 40 min compared to ~ 18 % of the 62.5 μg $mL^{-1}$ sample. The trend continued at 80 min where ~ 17 % of paraquat was removed, compared to ~ 20 % removed by the other. These results were compared to pristine MNPs, as elucidated in Fig. 9. In this case, the 82 μg $mL^{-1}$ sample (Fig. 9A) was active against paraquat removal only to a reduced extent compared to MNPs@Captisol. In particular, ~ 5 % and ~ 11 % at 40 min and 80 min were calculated, respectively. Only negligible paraquat adsorption (~ 0.6 % at 40 min and ~ 0.9 % at 80 min) for the 62.5 μg $mL^{-1}$ MNPs sample was observed (Fig. 9B). To understand whether the concentration of paraquat could influence the absorption kinetics, the experiment was repeated by keeping the concentration of MNPs@Captisol constant at 62.5 μg $mL^{-1}$ and changing that of paraquat (15 μM and 20 μM).

As elucidated by Fig. 8B, ~ 14 % and ~ 10 % at 40 min and ~ 21 % and ~ 15 % at 80 min removal percentages of paraquat from 15 μM and 20 μM samples were recorded, respectively. Again, the 10 μM sample was more efficient removing ~ 20 % at 40 min and ~ 22 % at 80 min of the initial amount of paraquat.

Based on these results, it can be speculated that concentrations and time are leading factors for the water remediation process. Overall, the MNPs@Captisol assembly achieved the greatest efficiency in the time interval up to 40 min, while the reduced efficiency between 40 min and 80 min is justified by the intrinsic stability of the system ($t_{½}$ = 28 min at 62.5 μg $mL^{-1}$ concentration). The mechanism is most likely to be identified in non-specific electrostatic surface adsorption. Cyclodextrins are not the preferable hosts in aqueous solution for charged guests such as paraquat dichloride, although some examples with modified cyclodextrins that complexed paraquat hexafluorophosphate (non-competitive counterions) in organic solvents such as acetonitrile and acetone can

**Table 3**
Comparison of similar cyclodextrin-based magnetite nanocomposites for water remediation.

| *MNPs* | *CD* | *Covalent functionalization* | *Pollutant* | *Nanosystem conc. (mg mL $^{-1}$)* | *Reaction time (min)* | *Removal efficiency* | *Adsorption capacity (mg g$^{-1}$)* | *Ref.* |
|---|---|---|---|---|---|---|---|---|
| α-$Fe_2O_3$ + $Fe_3O_4$ | β-CD | Yes | Metanfetamine (1.34 μM) | 0.8 | 40 | ~ 50 % (0.67 μM) | – | [58] |
| $Fe_3O_4$ | Carboxymethyl-β-CD polymer (CMPCD) | No Co-precipitation | Bisphenol A (2.19 mM) | 12 | 20–30 | – | 12 | [59] |
| | | | $Pb^{2+}$ (0.965 mM) | | | – | 50 | |
| $Fe_3O_4$ | Triazinyl-β-CD | Yes | $Pb^{2+}$, $Cu^{2+}$, $Zn^{2+}$, $Co^{2+}$ (30 mg $L^{-1}$) | 0.1 | 120 | 94 % $Pb^{2+}$; 49 % $Cu^{2+}$; 44 % $Zn^{2+}$; 33 % $Co^{2+}$ | – | [60] |
| Mesoporous $Fe_3O_4$ clusters | β-CD | Yes | Bisphenol A (2.19 mM) | 10 | 40–130 | – | 52.7 | [61] |
| $Fe_3O_4$ | β-CD | No Co-precipitation | 1-naphtol (34.68 mM) | 0.5 | 180 | – | 60 | [62] |
| | | | $Co^{2+}$ (17.24 mM) | | 120 | – | 12 | |
| Oleate capped-$Fe_3O_4$ | Carboxymethyl-β-CD (CMCD) | No | Naphtalene and 2-naphtol (2.5–25 μM) | 2.5 | 2880 | – | – | [63] |
| | | | $As^{3+}$ (13.35–1600 μM) | | | – | 800 | |
| | | | $As^{5+}$ (13.35–801 μM) | | | – | 300 | |

be found in the literature [55]. Anyway, Captisol is a β-CD derivative functionalized with negative-charged sulfobutyl chains that can electrostatically interact with oppositely charged molecules. As demonstrated by ζ-potential measurements (*see paragraph 3.6*), the MNPs@Captisol assembly showed a slightly negative surface charge (ζ-potential ~ −9 mV) that allowed the sequestering process. In comparison, the positively charged pristine MNPs (ζ-potential is around + 30 mV) resulted in non-efficient paraquat removal. Indeed, an electrostatic repulsion process is reasonable to justify the reduced interaction because of the di-cationic nature of the paraquat dichloride molecule. As a proof of concept, it was performed a control experiment using 62.5 μg mL$^{-1}$ dispersion of MNPs@Captisol for the water remediation of the model negatively charged pollutant dye methyl orange. Results reported in Fig. S17 confirmed that the negatively charged molecule was not sequestered by the system. In 40 min of interaction and after the magnetic separation, the absorbance of the supernatant was perfectly overlapping the t = 0 min. Another experiment was performed to assess the complexation of free Captisol molecules with paraquat preparing three samples in which the molar ratio was 1:1, 1:2 and 2:1, respectively. The concentration of paraquat was kept constant (10 μM) while the concentration of Captisol was variable. Briefly, 30 μL of 1 mM paraquat aqueous stock solution were added to ~ 3 mL of 5 μM, 10 μM and 15 μM Captisol solutions, respectively. The solutions were magnetically stirred for 30 min and then UV/Vis absorption spectra were collected. Results depicted in Fig. S18 were in good accordance with a recent paper from Razuvaeva et al [56] for similar structures. As in their case, the greatest hypochromic shift in the absorption band related to the methyl viologen derivative was found in the Captisol/paraquat 1:2 mol ratio sample. They also studied the complex with NMR spectroscopy and compared it to another similar system [57] it is confirmed the probable formation of an electrostatic complex between the negatively charged sulfobutyl chains of Captisol and paraquat.

Compared to similar cyclodextrin-based magnetite nanocomposites for water remediation in the literature (see Table 3), the MNPs@Captisol assembly stands out for the simplicity of preparation (no covalent functionalization methods were used) and the low cost. Moreover, it was effective in a concentration (62.5 μg mL$^{-1}$) that is far away from other examples that are in the range of 0.1 – 2.5 mg mL$^{-1}$ but at the present state shows around 20 % paraquat removal efficiency. In the future perspective, some optimization of the experimental parameters might be explored to improve the efficiency of the system. Moreover, the MNPs@Captisol assembly was designed to interact with positive-charged molecules and although it is desirable to extend the application to other similar molecules this would exclude negative-charged pollutants.

## 4. Conclusions

In this paper, a magnetic supramolecular assembly based on iron oxide nanoparticles (MNPs) and sulfobutylether-β-cyclodextrin (Captisol) is presented. Compared to other literature examples, a single-step preparation procedure based on the self-assembly between low-cost precursors was pursued without preliminary covalent functionalization processes. The morphological analysis showed clusters of iron oxide nanoparticles covered by an organic thin layer of sulfobutylether-β-cyclodextrin, as supported by TGA evaluations. This did not alter the magnetic properties of bare MNPs and the assembly was further characterized by spectroscopic (FT-IR, X-ray Photoelectron and μXRF) techniques. This fine cyclodextrin-based coating was sufficient to revert the positive ζ-potential of bare MNPs to the negative value of free Captisol. Overall, the colloidal dispersion of the assembly was less stable than the precursor due to increased mean hydrodynamic diameter and reduced ζ-potential in absolute value but it showed water remediation properties towards paraquat, a model positive-charged pollutant. The sequestering mechanism, that is dependent from concentration and electrostatic interactions, was ascertained to be driven by electrostatic complexation.

## Funding sources

This work was supported by the Italian Ministero dell'Università e della Ricerca (MUR) Piano Nazionale di Ripresa e Resilienza (PNRR) through the European Union program NextGenerationEU with the "SiciliAn MicrOnanoTecH Research And innovation CEnter" (SAMOTHRACE) [ECS:00000022 – CUP:B63C22000620005] project; the Italian Ministero dell'Università e della Ricerca (MUR) Programma Operativo Nazionale (PON) "Ricerca e Innovazione" 2014–2020, Azione IV.5 "Dottorati e contratti di ricerca su tematiche Innovazione and green"; and the University of Catania through the "PIAno di inCEntivi per la RIcerca di Ateneo" (PIA.CE.RI.) 2024/2026, "MATeriali e

Tecnologie InNovative per l'AmbienTe e l'energiA" (MATTINATA) project.

## CRediT authorship contribution statement

**Nina Burduja:** Methodology, Investigation. **Giuseppe Nocito:** Writing – original draft, Visualization, Methodology, Investigation, Formal analysis, Data curation. **Mariachiara Trapani:** Validation. **Alberto Riminucci:** Methodology, Investigation. **Riccardo Di Corato:** Methodology, Investigation, Formal analysis. **Antonio Della Torre:** Investigation. **Angelo Nicosia:** Methodology, Investigation, Data curation. **Antonino Gulino:** Writing – review & editing, Methodology, Investigation, Formal analysis. **Placido Giuseppe Mineo:** Writing – review & editing, Supervision, Investigation, Formal analysis. **Antonino Mazzaglia:** Writing – review & editing, Validation, Supervision, Project administration, Funding acquisition, Formal analysis, Conceptualization.

## Declaration of competing interest

The authors declare that they have no known competing financial interests or personal relationships that could have appeared to influence the work reported in this paper.

## Acknowledgements

We would like to thank Ligand (San Diego, CA-USA) for gently gifting us the sulfobutylether-β-cyclodextrin (Captisol®). Authors thank the B.R.I.T. laboratory of the University of Catania for the availability of the XPS facility.

## Appendix A. Supplementary data

Supplementary data to this article can be found online at https://doi.org/10.1016/j.molliq.2025.127625.

## Data availability

Data will be made available on request.

## References

[1] A.V. Davis, R.M. Yeh, K.N. Raymond, Proc. Natl. Acad. Sci. 99 (2002) 4793.
[2] V. Villari, N. Micali, A. Nicosia, P. Mineo, Top. Curr. Chem. 379 (2021).
[3] J.-M. Lehn, Chem. Soc. Rev. 36 (2007) 151.
[4] P. Mineo, V. Villari, E. Scamporrino, N. Micali, J. Phys. Chem. B 119 (2015) 12345.
[5] A. Nicosia, F. Vento, G. Marletta, G.M.L. Messina, C. Satriano, V. Villari, N. Micali, M.T. De Martino, M.J.G. Schotman, P.G. Mineo, Nanomaterials (2021).
[6] G. Crini, Chem. Rev. 114 (2014) 10940.
[7] J. Wankar, N.G. Kotla, S. Gera, S. Rasala, A. Pandit, Y.A. Rochev, Adv. Funct. Mater. 30 (2020) 1909049.
[8] C.V. Pardeshi, R.V. Kothawade, A.R. Markad, S.R. Pardeshi, A.D. Kulkarni, P. J. Chaudhari, M.R. Longhi, N. Dhas, J.B. Naik, S.J. Surana, M.C. García, Carbohydr. Polym. 301 (2023) 120347.
[9] V.J. Stella, R.A. Rajewski, Int. J. Pharm. 583 (2020) 119396.
[10] V. De Leo, A.M. Maurelli, L. Giotta, L. Catucci, Colloids Surf. B Biointerfaces 218 (2022) 112737.
[11] P. Garg, B. Kaur, G. Kaur, G.R. Chaudhary, Adv. Colloid Interface Sci. 302 (2022) 102621.
[12] C. Gila-Vilchez, L. Rodriguez-Arco, M.C. Mañas-Torres, L. Álvarez de Cienfuegos, M.T. Lopez-Lopez, Curr. Opin. Colloid Interface Sci. 62 (2022) 101644.
[13] L. Rijns, M.G.T.A. Rutten, A.F. Vrehen, A.A. Aldana, M.B. Baker, P.Y.W. Dankers, Nanoscale 16 (2024) 16290.
[14] L. Yue, K. Yang, X.-Y. Lou, Y.-W. Yang, R. Wang, Matter 3 (2020) 1557.
[15] A. Nicosia, F. Vento, C. Satriano, V. Villari, N. Micali, L.M. Cucci, V. Sanfilippo, P. G. Mineo, ACS Appl. Nano Mater. 3 (2020) 1950.
[16] G. Nocito, R. Zribi, M. Chelly, L. Pulvirenti, G. Nicotra, C. Bongiorno, A. Arrigo, B. Fazio, G. Neri, F. Nastasi, S. Conoci, Nanoscale 16 (2024) 3571.
[17] L. Kobrina, V. Boiko, V. Shtompel, N. Hudzenko, S. Rogalsky, M. Frasinyuk, A. Kozitskiy, S. Riabov, J. Mol. Struct. 1309 (2024) 138137.
[18] L. Mezzina, A. Nicosia, F. Vento, G. De Guidi, P.G. Mineo, Nanomaterials 12 (2022).
[19] F. Vento, A. Nicosia, L. Mezzina, G. Raciti, A. Gulino, M. Condorelli, L. D'Urso, G. De Guidi, P. Mineo, Adv. Mater. Technol. 8 (2023).
[20] C. Sanchez, P. Belleville, M. Popall, L. Nicole, Chem. Soc. Rev. 40 (2011) 696.
[21] S. Gómez-Graña, J. Pérez-Juste, P. Hervés, Adv. Colloid Interface Sci. 288 (2021) 102338.
[22] A. Mazzaglia, M. Trapani, V. Villari, N. Micali, F.M. Merlo, D. Zaccaria, M. T. Sciortino, F. Previti, S. Patanè, L.M. Scolaro, J. Phys. Chem. C 112 (2008) 6764.
[23] G. Nocito, S. Petralia, M. Malanga, S. Béni, G. Calabrese, R. Parenti, S. Conoci, S. Sortino, ACS Appl. Nano Mater. 2 (2019) 7916.
[24] M. Trapani, A. Romeo, T. Parisi, M.T. Sciortino, S. Patanè, V. Villari, A. Mazzaglia, RSC Adv. 3 (2013) 5607.
[25] M. Trapani, A. Scala, P.G. Mineo, A. Pistone, A. Díaz-Moscoso, A. Fragoso, L. Monsù Scolaro, A. Mazzaglia, J. Mol. Liq. 336 (2021) 116880.
[26] A.-M. Hada, M. Potara, S. Astilean, A. Cordaro, G. Neri, M. Malanga, A. Nostro, A. Mazzaglia, A. Scala, A. Piperno, Carbohydr. Polym. 293 (2022) 119736.
[27] A. Mazzaglia, G. Di Natale, R. Tosto, A. Scala, G. Sortino, A. Piperno, M. P. Casaletto, A. Riminucci, M.L. Giuffrida, P.G. Mineo, V. Villari, N. Micali, G. Pappalardo, J. Colloid Interface Sci. 613 (2022) 814.
[28] R. Zagami, A. Barattucci, L. Monsù Scolaro, M. Viale, G. Raffaini, P. Maria Bonaccorsi, A. Mazzaglia, J. Mol. Liq. 389 (2023) 122841.
[29] V.F. Cardoso, A. Francesko, C. Ribeiro, M. Bañobre-López, P. Martins, S. Lanceros-Mendez, Adv. Healthc. Mater. 7 (2018) 1700845.
[30] M.I.A. Abdel Maksoud, A.M. Elgarahy, C. Farrell, A.a.H. Al-Muhtaseb, D.W. Rooney, A.I. Osman, Coordination Chemistry Reviews 403 (2020) 213096.
[31] Y. Wang, J.F. Wong, X. Teng, X.Z. Lin, H. Yang, Nano Lett. 3 (2003) 1555.
[32] S.S. Banerjee, D.-H. Chen, Chem. Mater. 19 (2007) 6345.
[33] Y. Zhou, C. Wang, F. Wang, C. Li, C. Dong, S. Shuang, Chin. J. Chem . 34 (2016) 599.
[34] B. Chen, T. Lin, H. You, L. Fang, C. Chu, J. Yang, S. Tong, Colloids Surf A Physicochem Eng Asp 652 (2022) 129861.
[35] B. Chen, S. Chen, M. Wen, J. Zhu, S. Tong, J. Mol. Liq. 391 (2023) 123362.
[36] A.-L. Lungoci, I.-A. Turin-Moleavin, A. Corciova, C. Mircea, A. Arvinte, A. Fifere, N. L. Marangoci, M. Pinteala, Mater. Sci. Eng. C 94 (2019) 608.
[37] D. Briggs, J.T. Grant, Surface analysis by Auger and X-Ray Photoelectron Spectroscopy. 2003.
[38] A. Gulino, Anal. Bioanal. Chem. 405 (2013) 1479.
[39] G. Greczynski, L. Hultman, Angew. Chem. Int. Ed. 59 (2020) 5002.
[40] A. Riminucci, M. Uhlarz, R. De Santis, T. Herrmannsdörfer, J. Appl. Phys. 121 (2017) 094701.
[41] G.F. Goya, T.S. Berquó, F.C. Fonseca, M.P. Morales, J. Appl. Phys. 94 (2003) 3520.
[42] C.J. Bae, Y. Hwang, J. Park, K. An, Y. Lee, J. Lee, T. Hyeon, J.G. Park, J. Magn. Magn. Mater. 310 (2007) e806.
[43] S.P.K. Gubin, A. Yu, G.B. Khomutov, G.Y. Yurkov, Russ. Chem. Rev. 74 (2005) 489.
[44] Q. Li, C.W. Kartikowati, S. Horie, T. Ogi, T. Iwaki, K. Okuyama, Sci. Rep. 7 (2017) 9894.
[45] L. Nalbandian, E. Patrikiadou, V. Zaspalis, A. Patrikidou, E. Hatzidaki, N. P. Christos, Curr. Nanosci. 12 (2016) 455.
[46] N. Khan, G. Slathia, A. Saneja, J. Mol. Liq. 391 (2023) 123348.
[47] A.P. Grosvenor, B.A. Kobe, M.C. Biesinger, N.S. McIntyre, Surf. Interface Anal. 36 (2004) 1564.
[48] H. Kohzadi, M. Soleiman-Beigi, Sci. Rep. 11 (2021) 24508.
[49] B. Lesiak, N. Rangam, P. Jiricek, I. Gordeev, J. Tóth, L. Kövér, M. Mohai, P. Borowicz 7 (2019).
[50] D. Wilson, M.A. Langell, Appl. Surf. Sci. 303 (2014) 6.
[51] Z. Mokadem, S. Mekki, S. Saïdi-Besbes, G. Agusti, A. Elaissari, A. Derdour, Arab. J. Chem. 10 (2017) 1039.
[52] D. Franco, R. Zagami, L.M. De Plano, N. Burduja, S.P. Guglielmino, L.M. Scolaro, A. Mazzaglia, Molecules (2023).
[53] R. Zagami, A. Rubin Pedrazzo, D. Franco, F. Caldera, L.M. De Plano, M. Trapani, S. Patanè, F. Trotta, A. Mazzaglia, Int. J. Pharm. 637 (2023) 122883.
[54] R.H. Bromilow, Pest Manag. Sci. 60 (2004) 340.
[55] G. Cafeo, C. Gargiulli, G. Gattuso, F.H. Kohnke, A. Notti, S. Occhipinti, S. Pappalardo, M.F. Parisi, Tetrahedron Lett. 43 (2002) 8103.
[56] Y. Razuvaeva, R. Kashapov, A. Ziganshina, N. Kashapova, V. Salnikov, L. Zakharova, Carbohydr. Polym. 334 (2024) 121984.
[57] M.E. Flores, N. Sano, R. Araya-Hermosilla, T. Shibue, A.F. Olea, H. Nishide, I. Moreno-Villoslada, Dyes Pigm. 112 (2015) 262.
[58] P. Mayorga–Burrezo, C.C. Mayorga–Martinez, M. Kuchař, M. Pumera, Small 20 (2024) 2306943.
[59] A.Z.M. Badruddoza, Z.B.Z. Shawon, D.W.J. Tay, K. Hidajat, M.S. Uddin, J. Chem. Eng. 27 (2013) 69.
[60] A. Abdolmaleki, S. Mallakpour, S. Borandeh, RSC Adv. 5 (2015) 90602.
[61] J.H. Lee, S.-Y. Kwak, Appl. Surf. Sci. 467–468 (2019) 178.
[62] X. Zhang, Y. Wang, S. Yang, Carbohydr. Polym. 114 (2014) 521.
[63] R. Chalasani, S. Vasudevan, J. Mater. Chem. 22 (2012) 14925.